

Experimental magnetic form factors in $\text{Co}_3\text{V}_2\text{O}_8$: A combined study of *ab initio* calculations, magnetic Compton scattering, and polarized neutron diffraction

N. Qureshi*

*Institute for Materials Science, University of Technology, Petersenstrasse 23, D-64287 Darmstadt, Germany
and Institut Max von Laue-Paul Langevin, 6 rue Jules Horowitz, BP 156, 38042 Grenoble Cedex 9, France*

M. Zbiri, J. Rodríguez-Carvajal, A. Stunault, E. Ressouche, T. C. Hansen, M. T. Fernández-Díaz, and M. R. Johnson
Institut Max von Laue-Paul Langevin, 6 rue Jules Horowitz, BP 156, 38042 Grenoble Cedex 9, France

H. Fuess

Institute for Materials Science, University of Technology, Petersenstrasse 23, D-64287 Darmstadt, Germany

H. Ehrenberg

Institute for Complex Materials, IFW Dresden, D-01069 Dresden, Germany

Y. Sakurai and M. Itou

Japan Synchrotron Radiation Research Institute (JASRI), SPring-8, Sayo, Hyogo 679-5198, Japan

B. Gillon

Laboratoire Léon Brillouin (CEA-CNRS), CE Saclay, 91191 Gif-sur-Yvette, France

Th. Wolf

Research Center Karlsruhe, Institute of Solid State Physics, D-76021 Karlsruhe, Germany

J. A. Rodríguez-Velamazán and J. Sánchez-Montero

*Instituto de Ciencia de Materiales de Aragón (CSIC-Universidad de Zaragoza), 50009 Zaragoza, Spain
and Institut Max von Laue-Paul Langevin, 6 rue Jules Horowitz, BP 156, 38042 Grenoble Cedex 9, France
(Received 25 July 2008; revised manuscript received 9 February 2009; published 18 March 2009)*

We present a combination of *ab initio* calculations, magnetic Compton scattering, and polarized neutron experiments, which elucidate the density distribution of unpaired electrons in the kagome staircase system $\text{Co}_3\text{V}_2\text{O}_8$. *Ab initio* wave functions were used to calculate the spin densities in real and momentum spaces, which show good agreement with the respective experiments. It has been found that the spin polarized orbitals are equally distributed between the t_{2g} and the e_g levels for the spine (*s*) Co ions while the e_g orbitals of the cross-tie (*c*) Co ions only represent 30% of the atomic spin density. Furthermore, the results reveal that the magnetic moments of the cross-tie Co ions, which are significantly smaller than those of the spine Co ions in the zero-field ferromagnetic structure, do not saturate by applying an external magnetic field of 2 T along the easy axis *a*. In turn, the increasing bulk magnetization, which can be observed by field dependent macroscopic measurements, originates from induced magnetic moments on the O and V sites. The refined individual magnetic moments are $\mu(\text{Co}_c)=1.54(4)\mu_B$, $\mu(\text{Co}_s)=2.87(3)\mu_B$, $\mu(\text{V})=0.41(4)\mu_B$, $\mu(\text{O1})=0.05(5)\mu_B$, $\mu(\text{O2})=0.35(5)\mu_B$, and $\mu(\text{O3})=0.36(5)\mu_B$ combining to the same macroscopic magnetization value, which was previously only attributed to the Co ions.

DOI: [10.1103/PhysRevB.79.094417](https://doi.org/10.1103/PhysRevB.79.094417)

PACS number(s): 75.25.+z, 75.30.Et, 75.30.Gw

I. INTRODUCTION

$\text{Co}_3\text{V}_2\text{O}_8$ represents the 3*d* transition-metal ortho-oxovanadates labeled as kagome staircase structures, and crystallizes in the orthorhombic space-group *Cmca*.^{1,2} Its crystallographic structure is characterized by edge-sharing CoO_6 octahedra forming buckled layers of corner-sharing triangles, the kagome staircases, which are separated along the *b* axis by VO_4 tetrahedra (Fig. 1).

The magnetic exchange is effectuated by a 90° Co-O-Co intralayer pathway. Interestingly, this system exhibits a sequence of five magnetic phase transitions featuring temperature-dependent incommensurate antiferromagnetic phases with commensurate lock ins and a ferromagnetic

ground state, where all magnetic structures are collinear along the *a* axis.³ The ferromagnetic structure reveals two strongly different magnetic moments for the cross-tie Co ions (4*a* site) and spine Co ions (8*e* site) of $1.54\mu_B$ and $2.73\mu_B$,³ respectively, despite the fact that both Co^{2+} ions apparently present high-spin configurations as macroscopic measurements exhibit saturation of the cross-tie moments.⁴ In the kagome staircase structure several nearest- and next-nearest-neighbor exchange interaction pathways are possible,³ which is the motivation for this study. Investigating the magnetization density, which is reflected by the respective magnetic form factors of the ions, may reveal preferred exchange pathways with the presence of

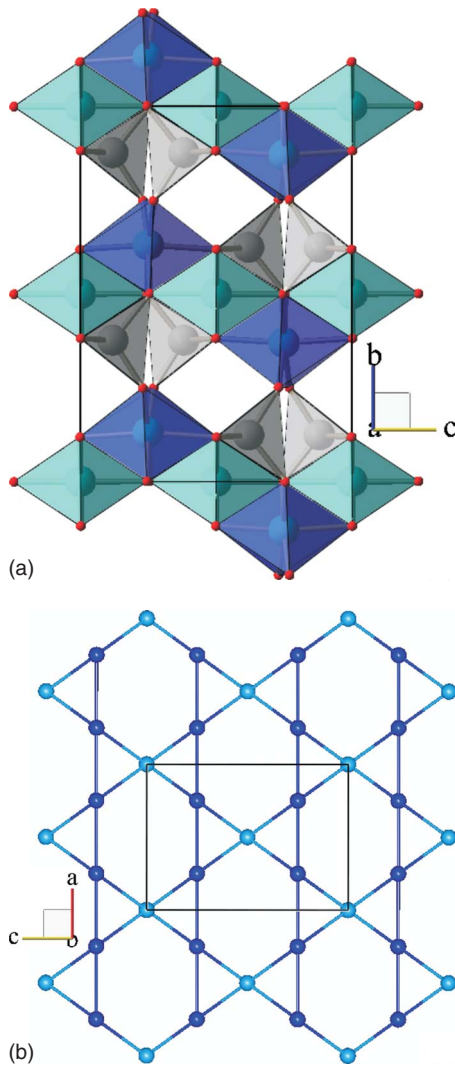


FIG. 1. (Color online) Visualization of the kagome staircase structure of $\text{Co}_3\text{V}_2\text{O}_8$. (a) shows the edge-sharing MO_6 octahedra [Co_cO_6 light blue (light gray), Co_3O_6 dark blue (dark gray)] isolated by nonmagnetic VO_4 tetrahedra (gray). (b) depicts a single kagome staircase viewed along the b axis with only the magnetic ions on both crystallographic sites [Co_c light blue (light gray), Co_3 dark blue (dark gray)].

magnetization on the involved O sites. Eventually induced magnetization on the empty d shell of V sites would allow interlayer coupling by superexchange. Therefore, magnetic Compton scattering (MCS) and polarized neutron-diffraction (PND) experiments have been carried out leading to the spin density in momentum space and the magnetization density in real space, respectively. However, detailed and precise analysis of these quantities are required in order to determine the exact contribution of the atomic species involved in the studied system. Quantum chemical modeling is therefore needed to gain insights, at a molecular level, into the electronic structure of the two cobalt-oxide octahedra. In this context, *ab initio* cluster calculations were performed for the Co_cO_6 and Co_3O_6 octahedra yielding precise molecular orbitals (MO) and wave functions (wf). The latter were used to analyze the experimentally observed density distributions. The

refinement of the contribution of each MO/wf, at a quantum chemical level, to the real and momentum space densities simultaneously is a powerful procedure allowing interesting and valuable features of the magnetic form factors to be determined. Therefore, a unique method of analysis has been employed, where both the real and momentum space quantities have been refined using the same molecular-orbital model. The limited amount of accessible data with the polarized neutron-diffraction and magnetic Compton scattering techniques has been overcome by correlating the analysis of the respective observations so that the refinement of either quantity is stabilized by the other which guarantees a high degree of validity of the achieved results.

II. AB INITIO CALCULATIONS

The two different clusters Co_cO_6 and Co_3O_6 were modeled separately. The calculations were performed within the framework of the Kohn-Sham formulation of the density-functional theory using the PC GAMESS program.⁵ The functional B3LYP was employed to approximate the exchange-correlation interaction. The B3LYP is a hybrid functional, well adapted to study transition-metal compounds and magnetic interactions, in which a predefined amount of the exact Hartree-Fock exchange is added to the well-known pure density functionals.⁶⁻⁹ The atoms in the cluster were described using Ahlrich's pVDZ atomic-orbital (AO) basis set¹⁰ $\text{Co}(14s, 8p, 5d, 1p)/[5s, 2p, 2d, 1p]$, $\text{O}(7s, 4p, 1d)/[3s, 2p, 1d]$. The notations (klm) and $[klm]$ indicate the number of Gaussian-type orbitals and contracted Gaussian-type orbitals, respectively. In order to mimic the Madelung potential, the two quantum-mechanical clusters were surrounded by point charges (PC) according to the effective fragment potential method.¹¹ As previously reported for other systems,¹²⁻¹⁵ the choice of the embedding method was shown to be crucial for the physical meaning of the *ab initio* calculations. To avoid the electron density leaking out of the cluster, a boundary region has been introduced, which is formed by effective core potentials (ECP) placed in the nearest cationic positions around the cluster. Thus, the first coordination shell of Co^{2+} and V^{5+} ions has been described by ECPs according to the SBKJC ECP basis set.¹⁶ As native ECPs for Co and V do not treat the $3s$ and $3p$ electrons as core electrons, those ECPs would in fact be too compact due to the higher number of valence electrons. In order to overcome this problem the ECPs for Mg and Al have been used due to the fact that their ionic radii are closer to those of Co and V, respectively. Except for the $3d$ shells, the remaining electrons are replaced by an effective potential. Thus, 1565 PC ($3 \times 3 \times 3$ unit cells with the respective Co ion in the center) have been built to mimic the Madelung potential on the cluster. The MO coefficients relevant to the Co $3d$ were extracted from the simulations and used to model the magnetic Compton profiles (MCP) and the magnetic form factors.

III. EXPERIMENTAL

A. Unpolarized neutron diffraction

$\text{Co}_3\text{V}_2\text{O}_8$ single crystals have been grown from self-flux in a ZrO_2/Y crucible by the slow cooling method. Some of

the crystals have been ground and investigated at the high-flux neutron powder diffractometer D20 (Institut Laue Langevin, Grenoble) confirming the absence of parasitic phases. The nuclear structure of a chosen single crystal has been studied at the four-circle diffractometer D9 (Institut Laue Langevin, Grenoble). A set of more than 500 independent reflections up to $\sin \theta/\lambda=0.92$ has been measured using two different wavelengths in order to determine the extinction effects ($\lambda_1=0.835 \text{ \AA}$, $\lambda_2=0.512 \text{ \AA}$). The data collection has been performed in the paramagnetic phase at $T=13.5 \text{ K}$, which is just above the Néel temperature of 11.2 K . In order to reveal possible structural changes between the paramagnetic and the ferromagnetic phases due to structural phase transitions or magnetostriction, an additional nuclear structure investigation has been carried out at the single-crystal diffractometer D15 (Institut Laue Langevin, Grenoble) under the same experimental conditions as the polarized neutron-diffraction experiment (Sec. III B), i.e., at $T=3.5 \text{ K}$ with an applied magnetic field of $H=2 \text{ T}$ along the easy axis a and using a wavelength of $\lambda=0.854 \text{ \AA}$.

B. PND

The real-space magnetization density has been studied at the hot neutron spin polarized two-axis diffractometer 5C1 (Laboratoire Léon Brillouin, Saclay). Neutrons from the source are monochromated and polarized by the (111) reflection of a magnetized Heusler crystal Cu_2MnAl . The wavelength is 0.84 \AA , which corresponds to the maximum flux of the hot source and is ideal for studying large domains of reciprocal space. The polarization factor of the beam is $p=-0.88$. In order to fully magnetize the sample and avoid beam depolarization, a magnetic field of $H=2 \text{ T}$ has been applied along the easy axis a . The flipping ratios R [Eq. (1)], the ratios between the spin-up and spin-down intensities, of over 500 independent (hkl) reflections with $h=0,1,2$ have been measured in the ferromagnetic phase at $T=3.5 \text{ K}$:

$$R = \frac{(F_N^2 + q^2 F_M^2) p_p^+ + 2 F_N q^2 F_M p_m^+ + (1 - q^2) q^2 F_M^2 y_{pm}^-}{(F_N^2 + q^2 F_M^2) p_p^- + 2 F_N q^2 F_M p_m^- + (1 - q^2) q^2 F_M^2 y_{pm}^-}, \quad (1)$$

F_M and F_N denote the magnetic and nuclear structure factors. $q=\sin \alpha$ is a geometric factor with α being the angle between the scattering and the magnetization vectors. The parameters $p_{p/m}^\pm$ and y_{pm} are extinction correction factors of the respective cross sections according to Ref. 17.

C. X-ray MCS

The investigation of the spin density in momentum space has been carried out at the High Energy Inelastic Scattering beamline BL08W at SPring-8 in Hyogo, Japan. This beamline is designed for magnetic Compton scattering spectroscopy as it offers high energy elliptically polarized x rays emitted from an elliptic multipole wiggler. The incident photon beam with an energy range of $170\text{--}300 \text{ keV}$ is monochromated and focused by an asymmetric Johann-type monochromator using the Si (620) reflection. The sample magnetization is achieved with a superconducting magnet with a maximum field of 2.5 T and a minimum polarity-

switching time of 5 s . The backscattered photon energy is analyzed by a ten-segmented Ge solid-state detector positioned at a scattering angle of 178.4° . The experiment has been carried out with an incident photon energy of 176.3 keV , which gives a good compromise between the beam intensity and the scattering cross section. The initial interest of applying this method to $\text{Co}_3\text{V}_2\text{O}_8$ was to map the momentum space spin density of the ferromagnetic phase as a projection onto the b^*-c^* plane in order to gather information about the $3d$ electron-spin states and to correlate the results with those obtained from the polarized neutron-diffraction experiment but the experimental conditions and especially the large magnetic anisotropy of the system did not allow that. The minimal achievable sample temperature is approximately 5.6 K , i.e., close below the magnetic transition into the antiferromagnetic phase. It can be seen in the magnetic phase diagrams of $\text{Co}_3\text{V}_2\text{O}_8$ (Refs. 4 and 18) that at this temperature already weak magnetic fields applied along the b or c axis induce a magnetic phase transition into the antiferromagnetic phase while $H\parallel a$ stabilizes the ferromagnetic one. The necessity of applying a magnetic field of considerable strength, and therewith magnetizing the sample along the incident beam in order to increase the magnetic contribution to the scattering cross section beside the requirement of turning the sample about a vertical axis to be able to reconstruct the two-dimensional momentum density, led to a change in strategy. To make sure not to induce magnetic phase transitions by rotating the sample with respect to the field direction, the measurements have been carried out within the antiferromagnetic phase at $T=7.5 \text{ K}$ and by applying a magnetic field of $H=2 \text{ T}$ with the induced ferromagnetic component lying in the b - c plane. In addition to the trivial directions $[010]$ and $[001]$, four further directional MCPs J_{mag} in the p_y - p_z plane have been investigated. An additional profile has been measured along the $[100]$ direction by decreasing the applied magnetic field to 0.25 T . A directional MCP yields the projection of the spin momentum space density onto the scattering vector, which is by definition p_z :

$$J_{\text{mag}}(p_z) = \int_{-\infty}^{\infty} \int_{-\infty}^{\infty} |\chi_{\uparrow}(\mathbf{p})|^2 - |\chi_{\downarrow}(\mathbf{p})|^2 dp_x dp_y, \quad (2)$$

with $\chi_{\uparrow(\downarrow)}(\mathbf{p})$ denoting the momentum wf of an occupied majority (minority) spin state. The Compton profiles of the respective sample magnetization states have been recorded for 60 s , repeating the cycle $[+---+--+]$ multiple times.

IV. RESULTS

A. Nuclear structure and extinction

The nuclear structure investigation at 13.5 K on the four-circle diffractometer D9 confirmed the correct phase formation of the orthorhombic structure (space-group $Cmca$) with $a=6.015(3) \text{ \AA}$, $b=11.480(5) \text{ \AA}$, and $c=8.289(4) \text{ \AA}$. The observed integrated intensities have been corrected for absorption by applying the transmission factor integral $\exp[\mu(\bar{t}_{\text{in}} + \bar{t}_{\text{out}})]$, and analyzed by simultaneously fitting a structure model to both datasets with λ_1 and λ_2 using FULLPROF.¹⁹ The refinement process included the atomic po-

TABLE I. Structural parameters of the investigated $\text{Co}_3\text{V}_2\text{O}_8$ single crystal.

Atom	x	y	z	B (\AA^2)
Co1	0	0	0	0.27(10)
Co2	0.25	0.1328(7)	0.25	0.20(7)
V	0	0.3773	0.1204	0.30
O1	0	0.2489(3)	0.2700(4)	0.38(4)
O2	0	0.0008(4)	0.2448(4)	0.33(4)
O3	0.2702(3)	0.1185(3)	0.9990(2)	0.33(4)

Extinction parameters				
x_{11}	x_{22}	x_{33}		
1.0(1)	0.36(5)	0.6(1)		

sitions and isotropic temperature factors of Co and O plus three additional extinction parameters according to an anisotropic Shelx-type empirical extinction correction.²⁰ The atomic position and temperature factor of V have been fixed in all refinements because of its low coherent neutron-scattering cross section. The refined structural parameters ($R=5.3$) are listed in Table I.

In order to analyze the nuclear structure under identical conditions as the flipping ratio measurement ($T=3.5$ K, $H=2$ T), only those reflections have been measured for which the ratio γ between the magnetic and the nuclear structure factor has been derived from the observed flipping ratios. The ferromagnetic contribution to the integrated intensity I has been canceled out according to

$$I \sim F_N^2 + |\mathbf{Q}_M|^2 = F_N^2 + q^2 F_M^2 = F_N^2(1 + q^2 \gamma^2), \quad (3)$$

where \mathbf{Q}_M is the magnetic interaction vector. The subsequent refinement showed that no considerable change in the nuclear structure has taken place, i.e., the derivation of the F_M from observed flipping ratios by using the observed F_N at $T=13.5$ K is justified.

All low-angle nuclear reflections suffer considerably from extinction; therefore, special attention has been paid to the extinction of magnetic scattering. As the flipping ratio treatment uses the same extinction parameters for both nuclear and magnetic scatterings, it is important to verify if the extinction effects are indeed comparable. Therefore, three strong magnetic reflections have been measured as a function of applied magnetic field after the sample has been cooled in zero field to 3.5 K. Figure 2 shows the integrated intensities of three reflections after the nuclear contribution has been subtracted. The field dependence of the magnetic contribution reveals a surprising and interesting tendency: instead of increasing with increasing applied field, as one would expect if the cross-tie moments get saturated, the intensity of magnetic scattering drops significantly.

This observation can be explained with field dependent increase in primary extinction. At $H=0$ T the sample exhibits a multidomain state with presumably negligible extinction effects. By increasing the field the magnetic domains grow until they reach approximately the size of the structural domains. On reaching saturation at $H \approx 0.25$ T, the primary

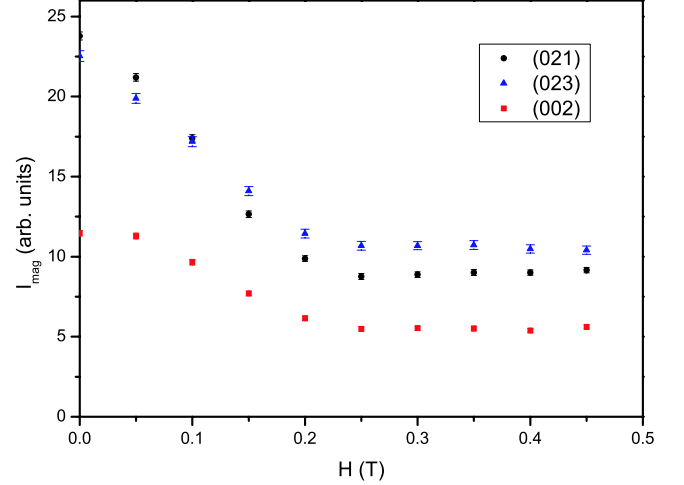


FIG. 2. (Color online) Intensity of three different magnetic reflections in dependence of an applied magnetic field revealing primary extinction effects.

extinction effects for magnetic scattering should be comparable to those of nuclear scattering. The mosaicity which governs secondary extinction should *a priori* not be affected. In order to verify these assumptions the extinction correction factor γ has been calculated for three magnetic reflections using the refined extinction parameters from the nuclear structure refinement according to the anisotropic FULLPROF model:

$$\gamma = \left[1 + \frac{0.001 F_M^2 \lambda^3 (x_{11} h^2 + x_{22} k^2 + x_{33} l^2)}{4 \sin^2(2\theta) (\sin \theta / \lambda)^2} \right]^{-1/2}. \quad (4)$$

The calculated values have been compared with the observed ones, which can easily be deduced from the intensity ratios at $H=0$ T and $H=0.25$ T. The results are listed in Table II. It can be seen that the calculated extinction factors are to a greater or lesser extent comparable with the observed ones. Nevertheless, the extinction of magnetic scattering seems to be underestimated.

B. Real-space magnetization density

The nuclear structure factors, which have been deduced from the unpolarized neutron experiments, have been used to derive the magnetic structure factors from the observed flipping ratios by solving Eq. (1) with respect to F_M . As the crystal structure is centrosymmetric the experimental magnetization density can directly be reconstructed by a Fourier

TABLE II. Observed and calculated extinction correction parameters for three low-angle magnetic reflections.

(hkl)	$\sin \theta / \lambda$ (\AA^{-1})	$F_{M, \text{obs}}$ (10^{-12} cm)	γ_{obs}	γ_{cal}
(021)	0.10595	4.87(1)	0.39(7)	0.46(3)
(002)	0.12064	3.39(1)	0.47(6)	0.64(3)
(023)	0.20083	4.72(1)	0.47(6)	0.60(3)

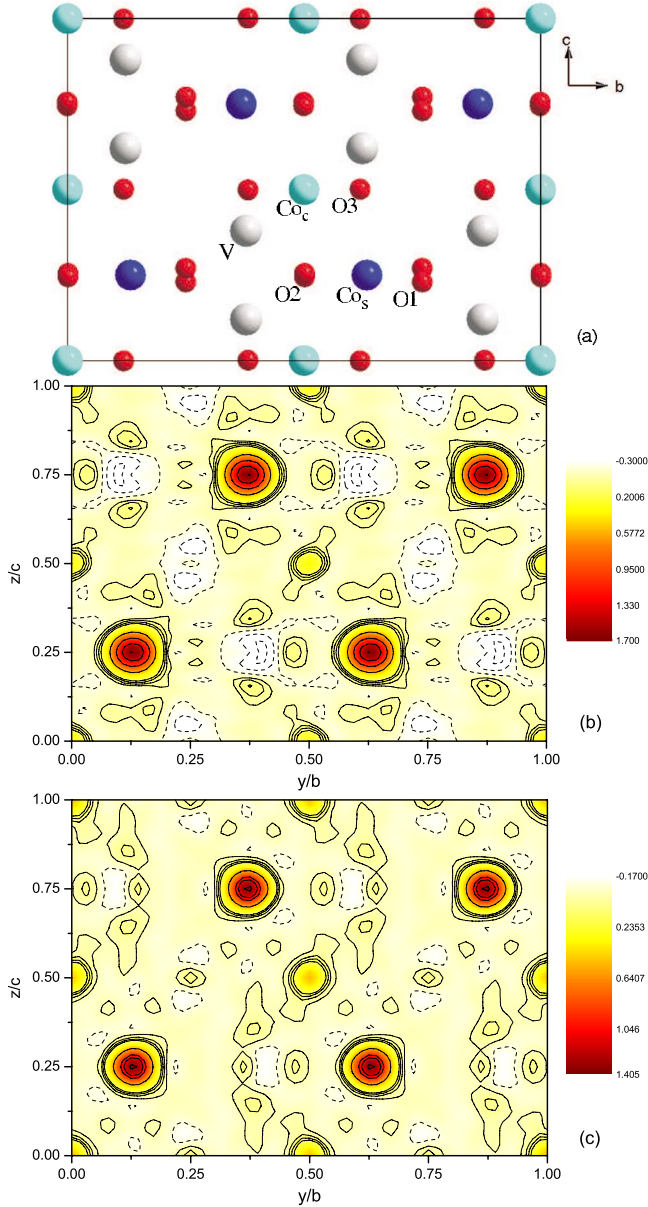


FIG. 3. (Color online) (a) Crystal structure viewed along the a axis. (b) Experimental and (c) calculated magnetization densities as a projection onto the b - c plane. Contour lines defining positive values are drawn as solid lines in $0.05\mu_B/\text{\AA}^2$ intervals between $0\mu_B/\text{\AA}^2$ and $0.15\mu_B/\text{\AA}^2$, and in $0.4\mu_B/\text{\AA}^2$ intervals above. Negative isodensities are represented by broken lines in $0.1\mu_B/\text{\AA}^2$ steps.

synthesis. Figure 3(b) shows the projection of the observed magnetization density onto the b - c plane while Fig. 3(a) depicts the unit cell viewed along the a axis in order to assign the density peaks to the respective atoms. Figure 3(c) represents the calculated magnetization density to which it will be referred in Sec. IV D. As it has been assumed in the previous section, the Co_c moments do not get saturated but significant magnetization density is present on V and O sites. While the density is quite localized for the V, O1, and O2 sites, rather diffused density can be observed around the O3 site. The split density peaks of O1 result from the fact that actually two O1 ions are visible in the projection. Similarly, the den-

TABLE III. Magnetic effects of the respective directional MCPs with a magnetic field H applied along the scattering vector. ϑ denotes the angle between a MCP and the $[001]$ direction.

MCP	ϑ ($^\circ$)	H (T)	M_0 (%)	S (μ_B)
[001]	0	2	0.541	0.616
[023]	17	2	0.488	0.556
[012]	34.7	2	0.415	0.472
[011]	54.1	2	0.274	0.312
[032]	64.3	2	0.229	0.261
[010]	90	2	0.095	0.108
[100]	90	0.25	0.251	0.287

sity around the Co_s ions seems to be much higher compared to the Co_c ions, which is due to the fact that two Co_s ions are contained in the projection while only one Co_c ion is projected. Besides the superexchange pathways Co_s -O2- Co_c and Co_s -O3- Co_c , an interlayer exchange becomes evident with the nonzero magnetization density of V and O1. Further *ab initio* solid-state computations are currently being performed to simulate the spin-density map of $\text{Co}_3\text{V}_2\text{O}_8$, and to elucidate the composite mechanisms of the induced magnetic moments on the different O and V sites. This will be the subject of a forthcoming publication.²¹

C. Momentum space density

The MCPs were extracted by taking the difference of the scattered intensities I^+ and I^- of the respective charge Compton profiles. Due to the fact that the more intense charge Compton profiles still exhibit relatively large values at the outermost measured positions of $p_z = \pm 10$ a.u. (atomic units), the actual number of electrons between -10 and $+10$ a.u. is evaluated from the profiles interpolated using tabulated data for the elements resulting from Hartree-Fock calculations.²² Before summing up the magnetic intensity of each detector cell, the data have been corrected for the detector cell efficiency, sample absorption, and scattering cross section according to Ref. 23. Furthermore, the energy scale of each detector cell has been calibrated by measuring a radioactive sample with well-known emission energies. The experimental MCPs were folded at $p_z=0$ to increase statistical accuracy by taking the average of each branch. The area under each profile has been normalized to the number of magnetic electrons per formula unit. With the use of iron standards the induced ferromagnetic component can be deduced from the magnetic effect, which is the relative contribution of the MCP to the total Compton profile

$$M_0 = \frac{I^+ - I^-}{I^+ + I^-} 100\%. \quad (5)$$

The magnetic effects of the respective directional MCPs are listed in Table III with their corresponding ferromagnetic components induced parallel to the scattering vector. In the p_y - p_z plane the spin moments monotonically decrease with increasing angle between the magnetic field direction and the $[001]$ direction, which directly reveals the magnetic aniso-

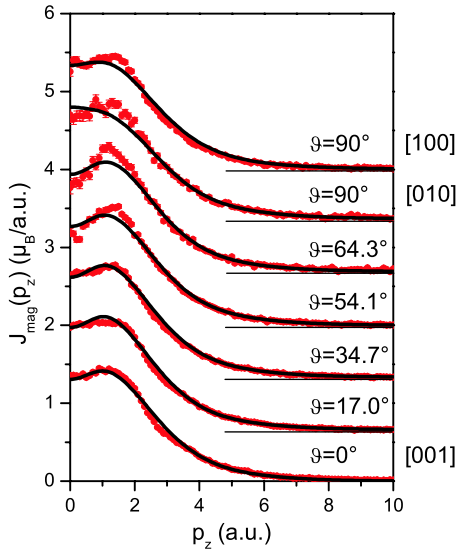


FIG. 4. (Color online) Observed (dots) and calculated (solid lines) normalized directional MCPs (shifted vertically in order to improve clarity, horizontal lines serve as a guide for the eye). The abscissa p_z is taken to be parallel to the respective scattering vector. ϑ denotes the angle between a respective MCP and the $\langle 001 \rangle$ direction.

tropy with b being the hard axis of this system.^{4,24} Effective beam path-length dependent multiple-scattering effects due to the rotation of the sample are estimated to be less than a few percent of the spin values given in Table III.

Figure 4 shows the normalized observed MCPs, which reveal similar shapes for the seven investigated crystallographic directions. Using all profiles except the one along the $[100]$ direction, the two-dimensional momentum spin density in the p_y - p_z plane has been reconstructed by the direct Fourier-transform method.^{25,26} The calculation has been performed on a grid with a distance of 0.1 a.u. between each point. The result is shown as a two-dimensional contour plot in Fig. 5(a). Low spin density can be recognized inside the first Brillouin zone (BZ), which extends beyond its border along the $\langle 010 \rangle$ and $\langle 001 \rangle$ directions. In the vicinity of the first BZ border the density increases more rapidly with increasing momentum along $\langle 021 \rangle$. Peaks are present at $(p_y, p_z) = (0.35, 1.85)$ and $(1.4, 0.55)$.

D. Correlated refinement in both spaces

The idea behind correlating the density distributions in real and momentum spaces is that the population of each spin polarized orbital must be represented likewise in the observed densities in both spaces. The fact that the MCS method only samples the spin part, and the PND method both the spin and the orbital parts of the magnetic moment has been handled in the following way. As the observed MCPs have been normalized, the area under each profile corresponding to the size of the spin moment is not refined. The refined parameters were the populations of each spin polarized orbital (in correlation with the real-space quantities), thus only the shape of each profile is refined. The refined magnetic moments stem solely from the PND data.

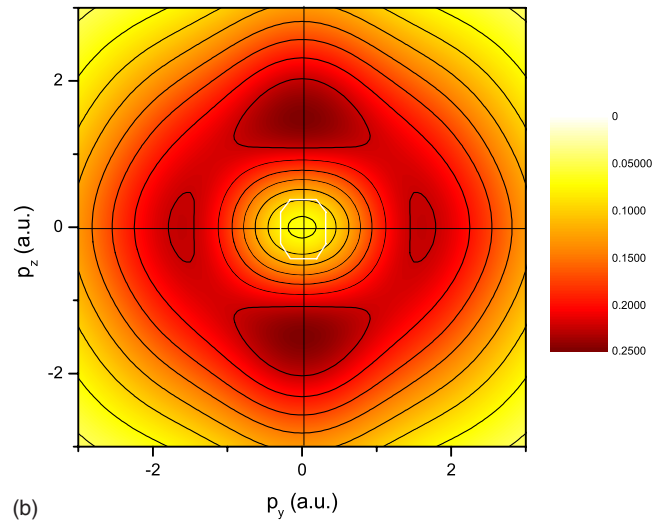
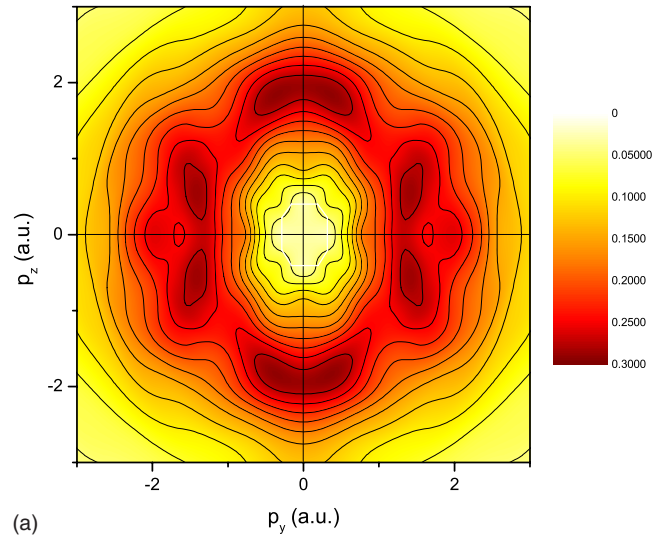


FIG. 5. (Color online) (a) Reconstructed experimental and (b) calculated spin momentum density in the p_y - p_z plane. Contours are drawn in $0.025\mu_B/(\text{a.u.})^3$ intervals. White solid lines depict the boundary of the first Brillouin zone.

This type of data analysis is not the crucial fact for attaining a correct solution but the simultaneous description of two complementary quantities by one and the same theoretical model assures a high degree of validity of the sensitive parameters, which describe the aspheric unpaired electron distribution.

In order to analyze the observed MCPs theoretical ones have been calculated by projecting the square of the *ab initio* wf onto the respective scattering vector. Thereby the symmetry relations between the different cluster density distributions in the unit cell have to be taken into account, which yields two and four symmetrically inequivalent Co_cO_6 and Co_sO_6 clusters, respectively (Table IV).

The point symmetries of the Co_cO_6 and Co_sO_6 clusters are $2/m..$ and $.2.$,²⁷ which correspond to $2/m..$ and $.2/m.$ in momentum space. Due to the special symmetry of the Co_sO_6 density, the projections of the different clusters in momentum space are invariant for the principal axes and those in the p_y - p_z plane. In the case of the Co_cO_6 clusters, the projections

TABLE IV. Symmetry relations between the two and four inequivalent Co_cO₆ and Co_sO₆, respectively.

Cluster	Co position	Symmetry relation to c_1/s_1
c_1	(0,0,0)	xyz
c_2	$(0, \frac{1}{2}, \frac{1}{2})$	$xy\bar{z}$
s_1	$(\frac{1}{4}, y, \frac{1}{4})$	xyz
s_2	$(\frac{3}{4}, y, \frac{1}{4})$	$\bar{x}yz$
s_3	$(\frac{3}{4}, \bar{y}, \frac{3}{4})$	$\bar{x}\bar{y}\bar{z}$
s_4	$(\frac{1}{4}, \bar{y}, \frac{3}{4})$	$x\bar{y}\bar{z}$

onto nonprincipal axes in the p_y - p_z yield different profiles, which need to be averaged. The projected orbitals have been convoluted with a Gaussian function having a full width at half maximum of the instrumental resolution. As reported previously²⁸ the fact that the projection of each MO in momentum space has a characteristic shape makes it possible to refine its population β_k which is the contribution to the observed MCP:

$$J_{\text{mag}}(p_z) = \int_{-\infty}^{\infty} \int_{-\infty}^{\infty} \sum_k \beta_k \chi_k^2(\mathbf{p}) dp_x dp_y. \quad (6)$$

Here, $\chi_k(\mathbf{p})$ denotes a momentum space MO/wf. Similarly, the populations β_k of the real-space MOs can be used to deduce the magnetic form factors $f_X(\mathbf{q})$ of the respective elements X by calculating the Fourier transform of the atomic spin density:

$$f_X(\mathbf{q}) = \int_{-\infty}^{\infty} \int_{-\infty}^{\infty} \int_{-\infty}^{\infty} \sum_k \beta_k \psi_{k,X}^2(\mathbf{r}) \exp(2\pi i \mathbf{q}\mathbf{r}) d\mathbf{r}, \quad (7)$$

where $\psi_{k,X}$ defines the real-space MO k only including the atomic orbitals $\phi_{i,X}$ of element $X=\text{Co}, \text{O}$. With this procedure the observed flipping ratios can be refined based on a simple aspheric magnetic form-factor model deduced from *ab initio* wf. For the V ions the analytic approximation of the V⁴⁺ form factor²⁹ has been used. Refining the population parameters for each MCP individually yields excellent agreement with the observed profiles. But since the refinement process exhibits numerous local minima with significantly varying results, it has been considered more reasonable to include all MCPs in the refinement despite the magnetic anisotropy. In doing so a global solution was found for the MCS data which satisfies—although to a lesser extent—the directional dependencies. The respective population parameters β_k have been refined simultaneously in both spaces together with the magnetic moments of Co, V, and O by minimizing the function

$$\chi^2 = \frac{1}{2} \sum_i \frac{(R_{i,\text{obs}} - R_{i,\text{cal}})^2}{\sigma_{i,\text{obs}}^2} + \frac{1}{2} \sum_n \sum_j \frac{[J_{n,\text{obs}}(p_{z,j}) - J_{n,\text{cal}}(p_{z,j})]^2}{\sigma_{j,\text{obs}}^2}, \quad (8)$$

with i and j defining discrete data points of the PND and MCS experiments, respectively, and n referring to the re-

TABLE V. Refined orbital occupation parameters of the Co_cO₆ and Co_sO₆ clusters.

Orbital	Co _c	Co _s
d_{xy}	0.27(2)	0.12(2)
d_{xz}	0.27(2)	0.12(2)
d_{yz}	0.16(2)	0.26(2)
$d_{x^2-y^2}$	0.17(2)	0.30(2)
$d_{3z^2-r^2}$	0.13(2)	0.20(2)

spective MCPs. No constraints have been set between the respective population parameters of the two different cluster molecular orbitals, i.e., according to Eq. (6) a linear combination of ten molecular orbitals with free refinable coefficients has been applied. The refinement yields fairly good agreement expressed by $R_{\text{MCS}}=5.7$ and $R_{\text{PND}}=9.6$ for the respective experiments. The refined total magnetic moments along the a axis are

$$\mu(\text{Co}_c) = 1.54(4) \mu_B,$$

$$\mu(\text{Co}_s) = 2.87(3) \mu_B,$$

$$\mu(\text{V}) = 0.41(4) \mu_B,$$

$$\mu(\text{O1}) = 0.05(5) \mu_B,$$

$$\mu(\text{O2}) = 0.35(5) \mu_B,$$

$$\mu(\text{O3}) = 0.36(5) \mu_B.$$

Summing the magnetic moments of all ions in the unit cell weighted by their site multiplicity and dividing by the number of Co ions yields an averaged magnetization of $3.45 \mu_B/\text{Co}^{2+}$. This value shows excellent agreement with the macroscopic magnetization for $H=2$ T along the a axis reported in Ref. 4. The resulting relative orbital populations are listed in Table V. The refined parameters were used to calculate the MCPs, which are depicted as solid lines in Fig. 4. Figure 6 shows that the line shapes of the two respective contributing parts (Co_cO₆ and Co_sO₆ MOs) are different concerning the ratio between the value at the peak and at $p_z=0$, and that they vary with the projection angle, which is important for a meaningful fit. Particularly the different directional variations in the individual orbital projections exclude misleading correlations between refined parameters (i.e., those orbitals whose projections on one scattering vector are similar), which is the reason why the inclusion of all observed MCPs in the refinement process favors a more stable fit. Figure 7 makes evident that refining the MCP along [001] (first column) individually causes the occupation parameters for the Co_c and the Co_s orbitals to be strongly correlated. By including those directional MCPs where the orbital projections are significantly different, the correlation is released and the refinement process converges toward a global minimum. Although Fig. 6 suggests that the Co_cO₆ and Co_sO₆ line shapes are similar, it can be seen in the lower line of Fig. 7 that even the equivalent orbital types have quite different

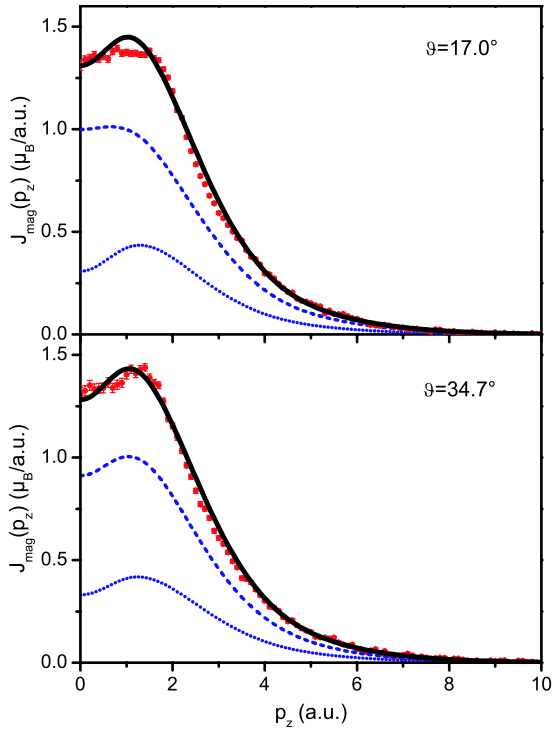


FIG. 6. (Color online) Observed (dots) and calculated (solid lines) MCPs along two different directions. The dotted and dashed lines show the contribution of the Co_cO_6 and the Co_sO_6 cluster, respectively.

characteristics in their line shapes which makes a differentiation possible. In this regard it is important to imply the real-space data which provide more information about the unpaired electron distribution compared to the linear projection of the momentum space quantities. An attempt to refine the theoretical model to the PND data individually yielded re-

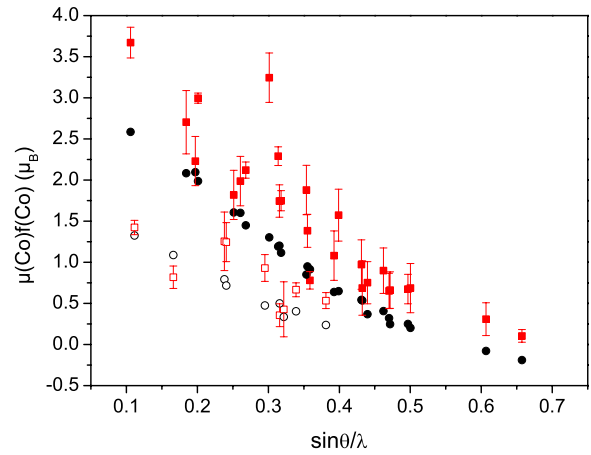


FIG. 8. (Color online) Observed (squares) and calculated (dots) magnetic form factors as a function of $\sin \theta/\lambda$. The calculated values represent exclusively the form factors of the Co_c (open symbols) and Co_s (filled symbols), which are accessible due to special reflection conditions. The discrepancies between the magnetic form-factor curves have to be attributed to induced magnetic moments on the V and O sites.

sults close to the ones presented above. As the magnetic structure factors, which can be deduced from the flipping ratios, contain a contribution from every species for all but two types of (hkl) reflections, only limited conclusion can be drawn concerning the observed magnetic form factors. Using the special reflection conditions of the $4a$ and $8e$ sites,²⁷ it is possible to draw the observed magnetic form factors of the Co_c and the Co_s ions individually assuming that no additional contribution stems from the V and O site, which are not subject to special conditions. In Fig. 8 these values are compared to the calculated ones—also only including Co—clearly exhibiting that the magnetic form factors are gener-

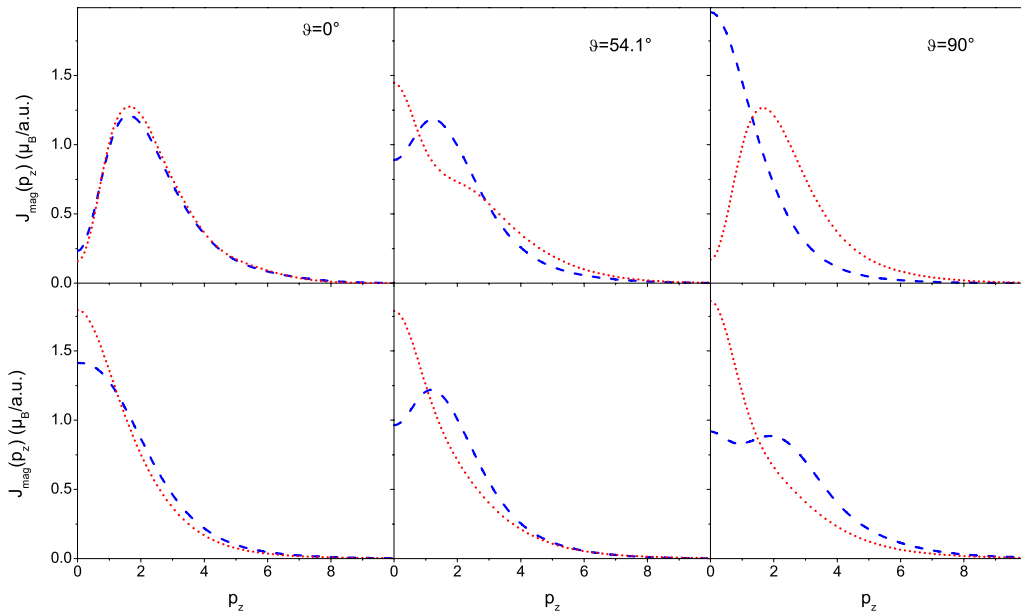


FIG. 7. (Color online) Co_c (broken line) and Co_s orbitals (dotted line) as a projection onto different scattering vectors revealing the different directional dependence of inequivalent (upper line, $\text{Co}_c d_{xz}$ and $\text{Co}_s d_{yz}$) as well as equivalent orbitals (lower line, d_{xy}).

ally underestimated, which fortifies the existence of magnetization on the V and O sites.

From the calculated MCPs the momentum space spin density has been reconstructed [Fig. 5(b)]. The calculated real-space magnetization density map [Fig. 3(c)] has been obtained by a Fourier synthesis of the calculated magnetic structure factors. The main features of the respective density maps coincide well although some differences are evident: the dip in the momentum space density around $p_z=0$ is not pronounced well in the calculated map and has a shape, which is rotated by 90° with respect to the observed map. This is connected to the less good fit of the magnetic Compton profiles below 3 a.u., and possibly results from strong hybridization effects between the Co $3d$ and O $2p$ orbitals. Furthermore, the disagreements between the experimental and calculated MCPs are most probably due to the limitation of the cluster calculations. Considering a larger sized cluster or the solid state, the gap between the experiment and fitting could be reduced. The real-space spin density of the O1 and O3 sites is slightly underestimated. Furthermore, density peaks exist next to the spine site density along the z axis, which do not coincide with atomic positions. However, this fact can be attributed to truncation effects in the Fourier series.

E. Discussion

The study presented here combining several methods reveals very interesting magnetic properties of the kagome staircase system $\text{Co}_3\text{V}_2\text{O}_8$. The previous assumption that the ferromagnetic structure at zero magnetic field is not fully ordered because of the Co_c only exhibiting $1.54\mu_B$ is disproved. Previous macroscopic magnetization measurements⁴ indeed showed a saturated moment of approximately $3.4\mu_B$ per Co site at $H=2$ T along a but the results of the polarized neutron single-crystal diffraction experiment with adequate extinction correction presented here reveal that the field dependent increase in magnetization stems from induced magnetic moments on the V, O2, and O3 sites; the Co moments remain practically unchanged from the values given for the zero-field magnetic structure.³ Hereby, the V and O2 sites show quite localized magnetization density while the O3 density seems to be smeared out due to truncation effects in

the Fourier series. A periodic *ab initio* calculation confirms the existence of magnetization density on the V and O sites and will be presented elsewhere.²¹ The spin polarized density on O2 and O3, which are those oxygen ions in the Co_cO_6 clusters, may be a strong indication for a partially covalent character of the Co_c ions and the reason for their relatively low magnetic moment compared to Co_s . The magnetization density distribution clearly exhibits the superexchange pathways between the two different Co sites but it indicates also the interlayer coupling, which is mediated by the V-O1 bridge. Combining the methods of polarized neutron diffraction and magnetic Compton scattering allowed us to refine the occupations of the Co $3d$ orbitals in a stable way. Like it has been previously reported but with inverted values,³⁰ the two crystallographically different Co ions exhibit different spin polarized orbital occupations. While the unpaired electrons are equally distributed between the t_{2g} and e_g levels for the Co_s ion, the magnetic signal stems by only 30% from the e_g orbitals for the Co_c ion as a consequence of the spin transfer from the surrounding O ions. Concerning the e_g orbitals of both ions the basal plane orbital $d_{x^2-y^2}$ is more populated than the apical $d_{3z^2-r^2}$ orbital. This possibly indicates a higher exchange interaction between the Co_s ions via an intermediate O2 ion. In the case of the Co_c ions it could be a hint that the magnetic exchange with the spine Co ions takes place preferentially via an O3 ion. The fact that the $\text{Co}_3\text{V}_2\text{O}_8$ compound exhibits magnetization on the oxygen ions similar to previously investigated systems³¹⁻³³ seems obvious but exact quantification of the induced magnetic moments is necessary. An adequate method for probing element specific spin and orbital magnetic moments is the x-ray magnetic circular dichroism, which should be employed shortly in order to confirm the values presented here.

ACKNOWLEDGMENTS

This research was supported by the Deutsche Forschungsgemeinschaft within the priority program 1178. The magnetic Compton scattering experiment was performed with the approval of the Japan Synchrotron Radiation Research Institute (JASRI) (Proposal No. 2007B2021). Helpful discussions with A. A. Granovsky and A. Koizumi are thankfully acknowledged.

*Corresponding author; navidq@st.tu-darmstadt.de

¹H. Fuess, E. F. Bertaut, R. Pauthenet, and A. Durif, *Acta Crystallogr., Sect. B: Struct. Crystallogr. Cryst. Chem.* **26**, 2036 (1970).

²E. E. Sauerbrei, R. Faggiani, and C. Calvo, *Acta Crystallogr., Sect. B: Struct. Crystallogr. Cryst. Chem.* **29**, 2304 (1973).

³Y. Chen *et al.*, *Phys. Rev. B* **74**, 014430 (2006).

⁴N. R. Wilson, O. A. Petrenko, and G. Balakrishnan, *J. Phys.: Condens. Matter* **19**, 145257 (2007).

⁵A. V. Nemukhin, B. L. Grigorenko, and A. A. Granovsky, *Moscow Univ. Chem. Bull. (Engl. Transl.)* **45**, 75 (2004).

⁶A. D. Becke, *J. Chem. Phys.* **98**, 5648 (1993).

⁷C. Lee, W. Yang, and R. G. Parr, *Phys. Rev. B* **37**, 785 (1988).

⁸B. Miehlisch, A. Savin, H. Stoll, and H. Preuss, *Chem. Phys. Lett.* **157**, 200 (1989).

⁹P. J. Stephens, F. J. Devlin, C. F. Chabalowski, and M. J. Frisch, *J. Phys. Chem.* **98**, 11623 (1994).

¹⁰A. Schäfer, H. Horn, and R. Ahlrichs, *J. Chem. Phys.* **97**, 2571 (1992).

¹¹M. S. Gordon, M. A. Freitag, P. Bandyopadhyay, J. H. Jensen, V. Kairys, and W. J. Stevens, *J. Phys. Chem. A* **105**, 293 (2001).

¹²E. Radzhabov and M. Kirm, *J. Phys.: Condens. Matter* **17**, 5821 (2005).

¹³J. L. Pascual, J. Schamps, Z. Barandiarán, and L. Seijo, *Phys.*

- Rev. B **74**, 104105 (2006).
- ¹⁴Z. Barandiarán and L. Seijo, *J. Chem. Phys.* **89**, 5739 (1988).
- ¹⁵J. L. Pascual, L. Seijo, and Z. Barandiarán, *J. Chem. Phys.* **98**, 9715 (1993).
- ¹⁶W. J. Stevens and M. Krauss, *Can. J. Chem.* **70**, 612 (1992).
- ¹⁷M. Bonnet, A. Delapalme, P. Becker, and H. Fuess, *Acta Crystallogr., Sect. A: Cryst. Phys., Diffr., Theor. Gen. Crystallogr.* **32**, 945 (1976).
- ¹⁸N. Qureshi, H. Fuess, H. Ehrenberg, T. C. Hansen, and D. Schwabe, *Solid State Commun.* **142**, 169 (2007).
- ¹⁹J. Rodríguez-Carvajal, *Physica B* **192**, 55 (1993).
- ²⁰A. C. Larson, in *Crystallographic Computing*, edited by F. R. Ahmed, S. R. Hall, and C. P. Huber (Munksgaard, Copenhagen, 1970), pp. 291–294.
- ²¹M. Zbiri, N. Qureshi, M. R. Johnson, H. Fuess, and H. Ehrenberg, (unpublished).
- ²²F. Biggs, L. B. Mendelsohn, and J. B. Mann, *At. Data Nucl. Data Tables* **16**, 201 (1975).
- ²³E. Żukowski, in *X-ray Compton Scattering*, edited by M. J. Cooper, P. E. Mijnarends, N. Shiotani, N. Sakai, and A. Bansil (Oxford University Press, New York, 2004), p. 133.
- ²⁴G. Balakrishnan, O. A. Petrenko, M. R. Lees, and D. M. K. Paul, *J. Phys.: Condens. Matter* **16**, L347 (2004).
- ²⁵R. Suzuki, M. Osawa, S. Tanigawa, M. Matsumoto, and N. Shiotani, *J. Phys. Soc. Jpn.* **58**, 3251 (1989).
- ²⁶Y. Tanaka, Y. Sakurai, A. T. Stewart, N. Shiotani, P. E. Mijnarends, S. Kaprzyk, and A. Bansil, *Phys. Rev. B* **63**, 045120 (2001).
- ²⁷*International Tables for Crystallography, Volume A: Space Group Symmetry*, edited by T. Hahn (D. Reidel Publishing, Boston, 1983).
- ²⁸A. Koizumi, S. Miyaki, Y. Kakutani, H. Koizumi, N. Hiraoka, K. Makoshi, N. Sakai, K. Hirota, and Y. Murakami, *Phys. Rev. Lett.* **86**, 5589 (2001).
- ²⁹E. J. Lisher and J. B. Forsyth, *Acta Crystallogr., Sect. A: Cryst. Phys., Diffr., Theor. Gen. Crystallogr.* **27**, 545 (1971).
- ³⁰H. Fuess, R. Müller, D. Schwabe, and F. Tasset, *J. Phys. C* **7**, 253 (1982).
- ³¹V. C. Rakhecha and N. S. Satya Murthy, *J. Phys. C* **11**, 4389 (1978).
- ³²M. Bonnet, A. Delapalme, H. Fuess, and P. Becker, *J. Phys. Chem. Solids* **40**, 863 (1979).
- ³³W. Lottermoser and H. Fuess, *Phys. Chem. Miner.* **19**, 46 (1992).